NUCL SCI TECH (2021) 32:60
https://doi.org/10.1007/s41365-021-00895-x

Development and high-gradient test of a two-half accelerator structure

Mao-Mao Peng[1,2] · Jia-Ru Shi[1,2] · Hao Zha[1,2] · Xian-Cai Lin[1,2] · Ze-Ning Liu[1,2] · Yu-Liang Jiang[1,2] · Jian Gao[1,2] · Liu-Yuan Zhou[1,2] · Fo-Cheng Liu[1,2] · Xiang-Cong Meng[1,2] · Huai-Bi Chen[1,2]

Received: 29 December 2020 / Revised: 21 April 2021 / Accepted: 27 April 2021 / Published online: 12 June 2021

Abstract This paper reports on the design, fabrication, RF measurement, and high-power test of a prototype accelerator—such as 11.424 GHz with 12 cells—and a traveling wave of two halves. It was found that the unloaded gradient reached 103 MV/m during the high-power test and the measured breakdown rate, after 3.17×10^7 pulses, was 1.62×10^{-4}/pulse/m at 94 MV/m and a 90 ns pulse length. We thus concluded that the high-gradient two-half linear accelerator is cost-effective, especially in high-frequency RF linear acceleration. Finally, we suggest that silver-based alloy brazing can further reduce costs.

Keywords Two-half structure · Silver-based alloy brazing · Low cost · High gradient

1 Introduction

Two-half structure accelerators have attracted growing interest since the 1970s and are generally known as muffin-tin structures [1]. The open nature of this structure provides various fabrication advantages [2]. Such a geometry allows ideal electropolishing configuration and relatively easy cleaning due to the absence of hidden areas or weld cracks. The ease of assembly makes it well suited for high-frequency accelerators, especially W-band and sub-THz accelerators [3–10].

Another important characteristic of the two-half structure is that no current can flow at the brazing joint [11], which allows different open structures—such as accelerators of quadrants [12] and PETS (Power Extraction and Transfer Structures), constructed from octants [13]—to be developed. A tunable accelerating structure made of two halves has been designed and fabricated for a Compact Linear Collider (CLIC) [14], achieving a gradient of 100 MV/m at a BDR of 1.5×10^{-5}breakdowns/pulse/m after 1.5 billion pulses in the high-power test. An open structure with high-order mode (HOM) damping was designed [15] to satisfy the requirement for strong suppression of the long-range transverse wakefield of CLIC, establishing a new damping structure design, other than the choke mode [16–18] and damped detuned structures [19].

The two-half structure has a promising future and broad application scenarios due to its low cost, facile fabrication/assembly, and no current flow at the bounding. To explore the fabrication and brazing draft of a two-half accelerator, we designed a 12-cell accelerator made of two halves and, to reduce costs, a silver-based alloy was used during brazing. A high-power test was subsequently conducted.

In Sect. 2, we described the RF simulation before fabrication and mechanical design. Section 3 presents the lower-power RF measurement data after brazing and compares them with the simulations. Section 4 presents a brief introduction to the Tsinghua X-band high-power test stand (TpoT-X) and analyses of the high-gradient test data. The conclusions are presented in Sect. 5.

This work was supported by the National Natural Science Foundation of China (No. 11922504).

✉ Hao Zha
zha_hao@mail.tsinghua.edu.cn

1 Department of Engineering Physics, Tsinghua University, Beijing 10084, China

2 Key Laboratory of Particle and Radiation Imaging, Tsinghua University, Ministry of Education, Beijing 10084, China

2 Design and fabrication

In this manuscript, the two-half structure comprises 10 middle cells and 2 matching cells. The middle cell of this structure is scaled from 11.994 GHz, as designed in Ref. [15], to 11.424 GHz, and the high-order mode damping waveguides were removed. A gap was added to the cell edge owing to its interaction with the metal surface (metal-to-metal contact) and is not bonded as brazed metal has a poor performance during high-power operation [15, 20, 21]. The gap was set at 1 mm. Figure 1 shows the field distribution; the color bar on the wall of the middle cell in the eigenmode simulation is considered to an important factor in the breakdown rate (BDR). The HFSS code, including the modified Poynting vector distribution, was employed [22]. The maximum electric and magnetic fields are located on the edge of the iris and top of the cavity, respectively, while there is no electric or magnetic field in the gap. The distribution of the modified Poynting vector was similar to that of the electric field.

The dimensions and parameters of the middle cell are listed in Table 1. To have a $2\pi/3$ phase advance, the length of the cavity was set to 8.75 mm. The beam iris diameter of the middle cell was 6.62 mm, and the iris thickness was 1.754 mm. When the diameter of the resonant cavity is 18.78 mm, the resonant frequency of the cavity is 11.424 GHz. The filling time of a single cell is $\tau = W_e/P_{in} = 1.42\,\text{ns}$, where W_e denotes the cavity stored energy and P_{in} is the input power of the iris. The group velocity is calculated as $v_g = D/\tau = 0.0198\,\text{c}$, where D is the length of the cell. The required power of 100 MV/m accelerating gradients of the middle cell in the HFSS eigenmode solver simulation was 57.44 MW. The shunt impedance and r/Q of this simulation were 105 MΩ/m and 14,422 Ω/m, respectively. The surface electric peak field was 2.45 times that of an accelerating gradient. The surface magnetic peak field and surface modified peak Poynting vector over the accelerating gradient and square of accelerating gradient were 3.59 mA/V and 1.07 mA/V, respectively.

The vacuum model of this structure is shown in Fig. 2. From Fig. 2, we can see that there are a total of 10 regular cells and two matching cells in the simulation. The structure is a constant impedance accelerator; therefore, the iris diameter of the 10 regular cells is the same. To match the impedance of regular cells with a WR90 rectangular waveguide, the symmetry-matching cells are kept at the ends. Matching waveguides were designed between the matching cells and WR90 rectangular waveguides. The dimensions of the matching cells and matching waveguides were optimized for better matching and to reduce the reflection of the rectangular waveguide port to below −40 dB in the simulation. To cut off the radiofrequency fields, the diameter of the beam pipes at both ends was set to 4 mm. While cutting the radiofrequency inside the cavity and avoiding field enhancement, the gap between the two halves was designed to be 1 mm owing to experimental evidence indicating that the metal surfaces are in metal-to-metal contact but not bonded or brazed. Brazed metal exhibits poor performance during high-power operation [15, 20, 21]. The length of the entire structure, including 10 regular cells, 2 matching cells, and waveguides, was 123 mm.

The mechanical design of this structure is shown in Fig. 3. The bounding surface surrounds the cavities and gaps. To ensure a 1-mm gap between the two halves, the cavity plane was selected to be 0.5 mm lower than the bounding surface. For better alignment, the bottom and top parts had six locating holes. The top and bottom parts were kept the same, except for the brazing alloy slot. Both the width and depth of the brazing alloy slot were maintained at 1.1 mm, which is slightly larger than that of the 1-mm-diameter silver-copper alloy wire. The beam pipe at the ends of this structure should be in very good alignment for brazing installation and vacuum sealing.

To minimize misalignment, two matching steps are required for the final brazing: first, milling of the beam-pipe matching slot with a smaller diameter on both sides of the top and bottom part and brazing the top and bottom part together with location pins for better alignment. The depth of the beam-pipe matching slot is 3 mm. Second, the beam-pipe brazing slots are enlarged after brazing the top and bottom parts to the outside diameter of the beam pipe and brazing the CF35 flanges, beam pipes, WR90 rectangular waveguides, CERN radiofrequency flanges, and the structure body together. The fabricated two halves and entire structure after brazing are shown in Fig. 4a, b. The total length of the structure, including beam pipes and CF35 flanges, was 230 mm.

3 RF measurement

Low-power RF measurements were conducted at Tsinghua University with a four-port R&S ZVA 40 vector network analyzer (VNA). The two radiofrequency ports on the left side in Fig. 4b are combined as port 1 in the VNA, and the two ports on the right side are combined as port 2. The measured S_{11} and S_{21} after the final brazing are presented in Fig. 5. The measured S_{11} in Fig 5a is inconsistent with the simulation data at a frequency near 11.424 GHz, which might be caused by a machining error. However, the measured value of S_{21} in Fig. 5b is in good agreement with that of the simulation data. At 11.424 GHz, the measured S_{11} and S_{21} are − 20 dB and − 0.643 dB, while the

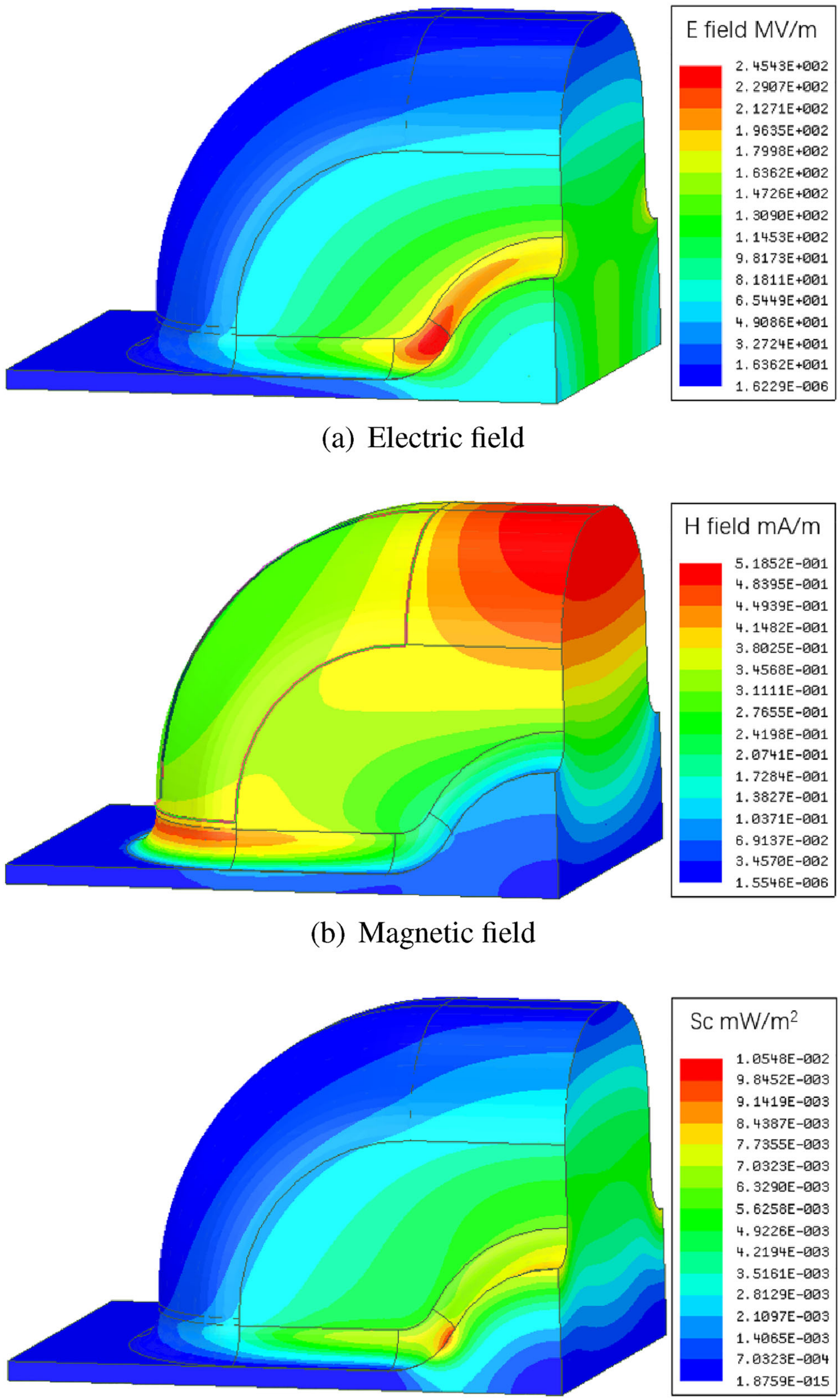

(a) Electric field

(b) Magnetic field

(c) Modified Poynting vector

Fig. 1 (Color online) **a** Electric field distribution, peak field located on the iris wall. **b** Magnetic field distribution and peak field located on the cavity wall. **c** Modified Poynting vector distribution of the middle cell surface. There was no electric field or magnetic field in the gap. All fields are normalized to a 100 MV/m accelerating gradient

Table 1 Parameters of middle cell normalized to 100 MV/m accelerating gradient

Parameters	Value
Frequency, f (GHz)	11.424
Iris diameter, $2a$ (mm)	6.62
Cavity diameter, $2b$ (mm)	18.78
Iris thickness, t (mm)	1.754
Cell length, D (mm)	8.75
Phase advance per cell, φ (rad)	$2\pi/3$
Filling time, τ (ns)	1.42
Group velocity, v_g (c)	0.0198
Input power, P_{in} (MW)	57.44
r/Q (Ω/m)	14,422.45
Shunt impedance, r_s (MΩ/m)	105
Surface electric field, E_s (MV/m)	245
Surface magnetic field, H_s (mA/m)	0.51
Surface modified Poynting vector, S_c (mW/m^2)	0.01

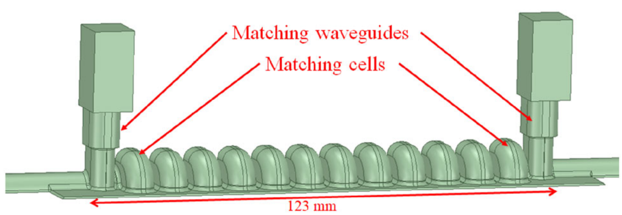

Fig. 2 (Color online) One-quarter vacuum part of two-half structure

simulation values are − 30 dB and − 0.76 dB. A 1% power reflection from the structure does not cause any damage to the pulse compressor and klystron.

A dielectric bead of 2 mm diameter was employed for bead-pulling. The VNA worked in continuous wave mode and was triggered by pushing the button. The dielectric bead was mounted on a fishing line and driven by a stepper motor. Simultaneously, the stepping motor was started and triggered the VNA. The square root of the measured S_{11} in the linear unit is the relative value of the on-axis field distribution. The bead-pulling [23] results are presented in Fig. 6, including the on-axis electric field distribution and phase advance per cell at 11.424 GHz. The voltage standing wave ratio of the on-axis electric field of all cells was 1.2; this demonstrates a relatively flat field distribution without tuning. The average phase advance per cell was measured as 117.2°, which is less than the designed value of 2.8°. The on-axis electric field distribution is measured in the range of 11.42–11.43 GHz. The phase advance versus frequency is shown as a dispersion curve in Fig. 7. The orange error bar in Fig. 7 refers to the standard deviation of the phase advance between cells, whereas the blue

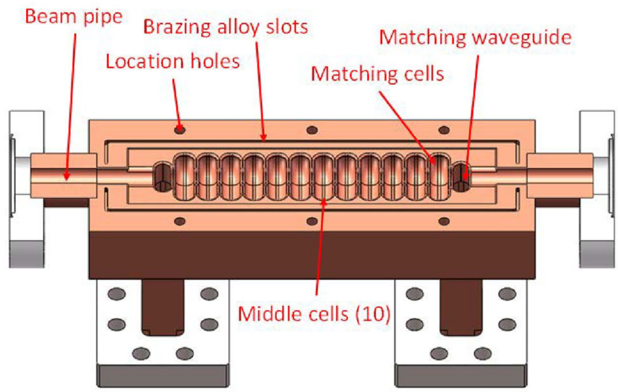

(a) Bottom part

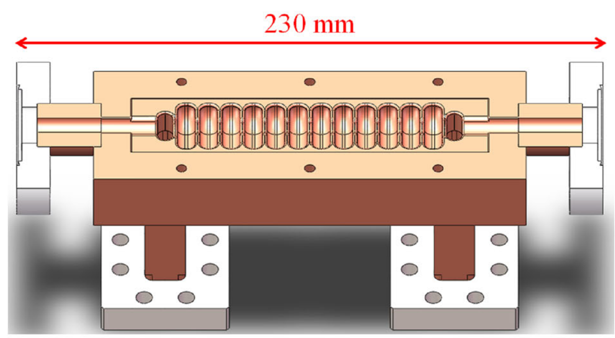

(b) Top part

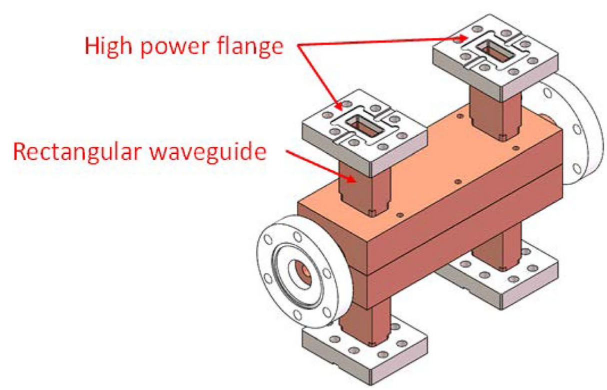

(c) Assembling of all parts

Fig. 3 (Color online) Mechanical design of the two-half structure. **a** Bottom part, **b** top part, and **c** assembly of all parts. The only difference between the two parts is the brazing alloy slot. Both parts have six locating holes for accurate alignment

error bar shows the minimum and maximum phase advance. The phase velocity is equal to the speed of light at 11.430 GHz, as shown in Fig. 7, which is 6 MHz higher than the designed value. All RF measurements were conducted in air at 24 °C.

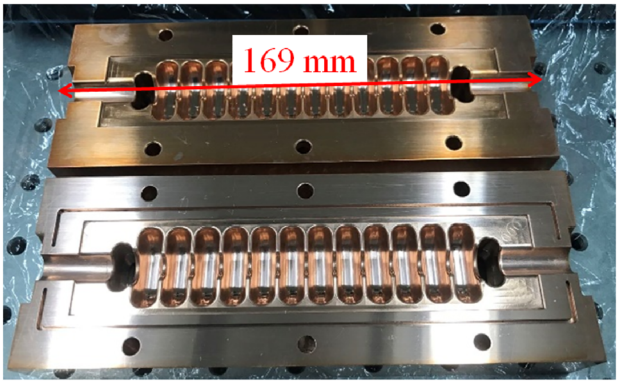

(a) Two open halves after machining and ultrasonic cleaning

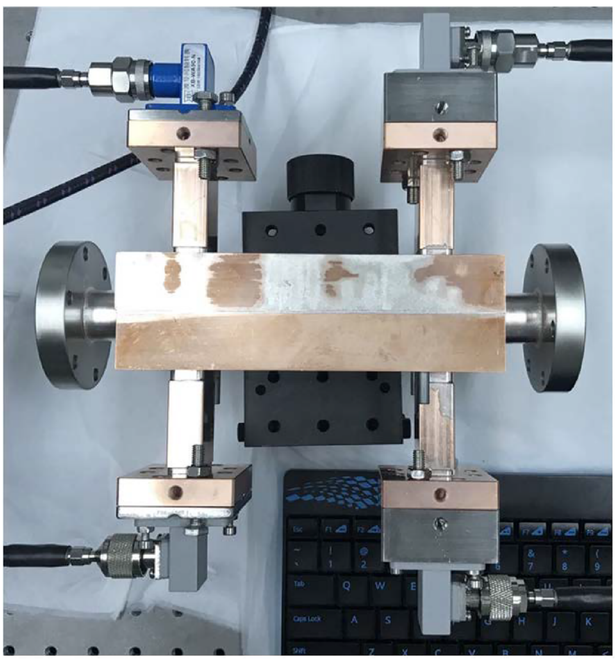

(b) The whole structure after brazing. RF measurements were performed, ready for the high-gradient test.

Fig. 4 (Color online) **a** Machined top and bottom part without beam pipes, flanges, and waveguides, **b** after brazing

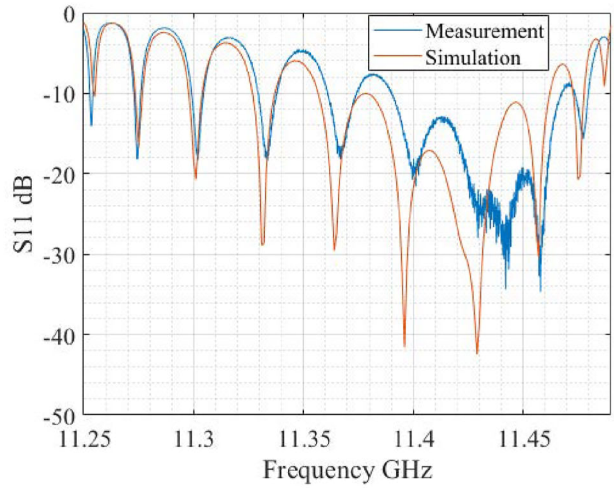

(a)

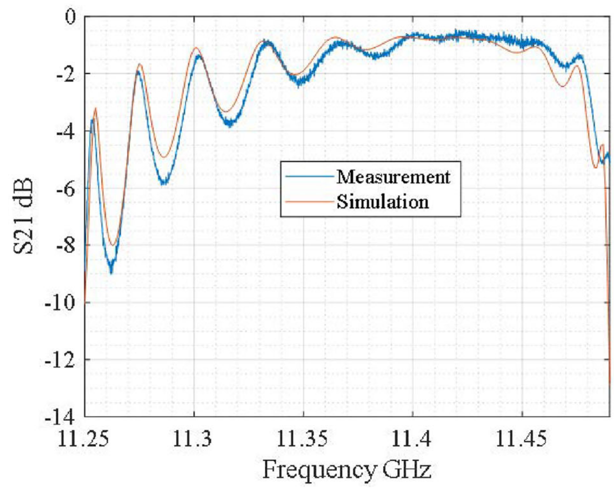

(b)

Fig. 5 (Color online) S parameters from measurement and simulation. **a** S11 from measurement and simulation; **b** S21 from measurement and simulation

4 High-power test

4.1 Tsinghua X-band high-power test stand

This two-half structure was tested via the Tsinghua X-band high-power test stand [24] (TpoT-X). A system diagram of TpoT-X is shown in Fig. 8. An R&S signal generator generates an 11.424 GHz radiofrequency pulse and drives the solid-state amplifier (SSA) using a coaxial cable. The maximum output pulse power of the solid-state amplifier is approximately 1.5 kW. A low-power waveguide system transports the output pulse of a solid-state amplifier to the CPI klystron. To eliminate the reflection of the klystron, isolators were installed before the klystron and after the solid-state amplifier. The maximum output power and pulse length of the klystron were 50 MW and 1.5 μs, respectively. The maximum repetition rate of the ScandiNova modulator was 40 Hz. The signal generator, solid-state amplifier, klystron, modulator, and electronic devices were placed outside of the shield room. The pulse compressor and undertesting devices were inside the shield room.

An automated conditioning system was used for this high-power test. The initial power, target power, etc., were set before operation. Initially, the power of the system increased to the target value at the initial pulse width. Then, the power was lowered and the pulse width was incremented until it reached the target power and pulse width. The system lowers the power and pauses in 10 s if a

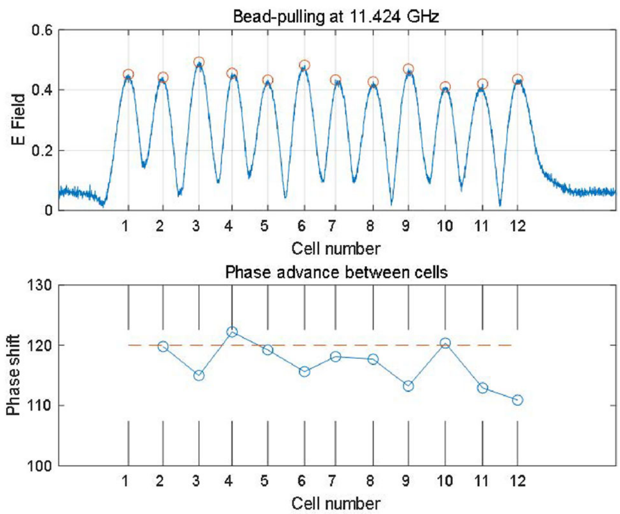

Fig. 6 (Color online) On-axis electric field distribution and phase advance

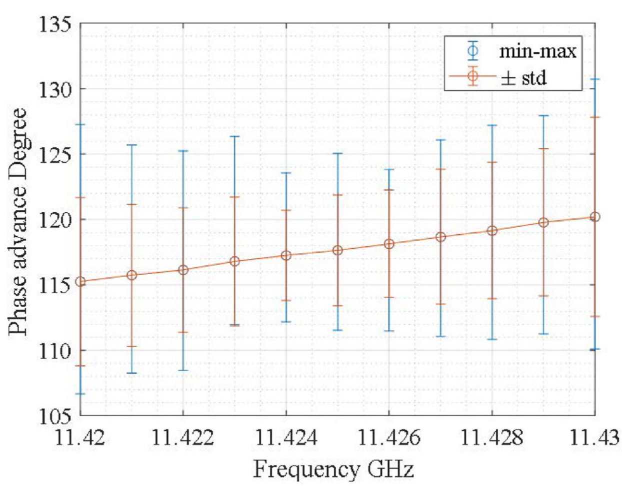

Fig. 7 (Color online) Dispersion curve measured by bead-pulling at frequencies ranges from 11.42 to 11.43 GHz. The phase velocity was equal to the speed of light at 11.430 GHz

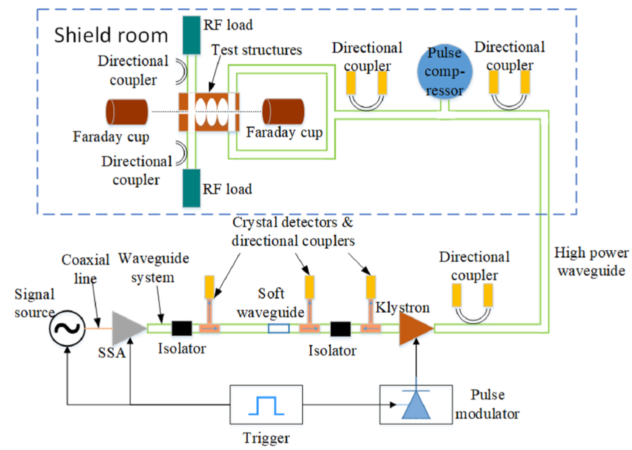

Fig. 8 (Color online) System diagram of Tsinghua high-power test stand with pulse compressor installed

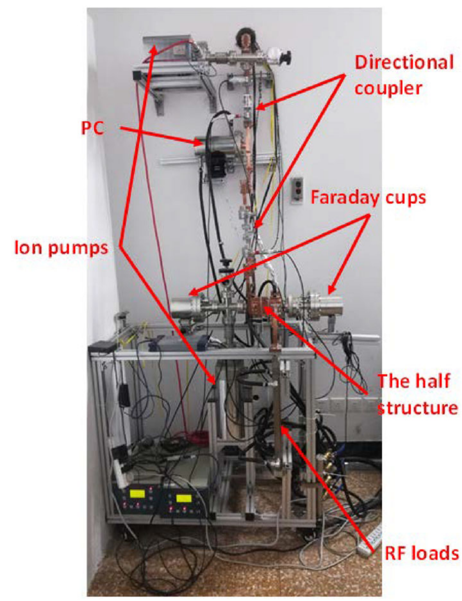

Fig. 9 (Color online) Tsinghua X-band high-power test in shielding room

breakdown occurs during conditioning. Normal waveforms were recorded each minute as single csv files (named as the time at which the file was saved). The pulse number, power, and vacuum pressures were measured by ion pumps, recorded in a separate text file.

A pulse compressor [25] was installed during this high-power test. The pulse width after the pulse compressor depends on the phase flipper, which is connected to the solid-state amplifier (SSA). During the high-power pulse compressor test, the peak power reached 150 MW.

To capture the dark current, two Faraday cups were installed in the up- and downstream port of the two-half structure, as shown in Fig. 9. Two stainless microwave loads were scaled from the S-band [26, 27], which absorbs the transmit power from the two-half structure. Reflected power measured by a directional coupler upstream of the two-half structure was used to interlock the auto-condition system as a breakdown criterion. For the transmit power and waveform measurements, another directional coupler was installed before one of the two RF loads. In addition to dark current and reflection power, this is an essential breakdown criterion. Radiofrequency waveforms and power were measured using Keysight crystal detectors. All crystal detectors were calibrated using a signal generator and scopes before the experiment.

4.2 Data analysis

Generally, there are two stages in conditioning history. Initial testing was performed without a pulse compressor, which was added partway through the test, as described in the next section. In the first stage, the klystron generates power and directly transmits it to a two-halve structure via a high-power waveguide. The input power of the two-half structure has a flat top, and a maximum pulse length of 200 ns is achieved during conditioning. To achieve higher power, a pulse compressor was installed before completion of the high-gradient test. Upon using a pulse compressor, the radiofrequency pulse achieved a sharp peak, followed by an exponential decay. The pulse length was compressed from 1.5 µs to 90 ns. The pulse length starts from 1/3 of the peak value to the end of the 1/3 peak value. Figure 10 shows the input radiofrequency power waveform, surface pulse heating, and gradient of the two-half structure. The entire structure is treated as a uniform transmission line in the time-domain gradient calculation, and radiofrequency power flows at the group velocity. The details of this method are described in [28]. From the comparison of Fig. 10a and b, we can conclude that even the compressed pulse has a higher effective power level. The pulse heating temperature was still lower than that without the pulse compressor; this is due to the short pulse, which has lower energy.

The pulse compressor was installed at 0.8×10^7 pulses, as shown in Fig. 11. The pulse length was increased from 50 to 200 ns with the help of conditioning logic, as described in the auto-condition system. After installation, the pulse length was maintained at 90 ns, and only the input power was increased. This structure had undergone 3.17×10^7 pulses in the whole procedure, which is far less than the pulse number in normal high-gradient tests [18, 29, 30]. The accelerating gradient in Fig. 11 was calculated pulse by pulse. At the end of this high-power test, we measured the breakdown rate of the first cell gradient—84 MV/m, 88 MV/m, and 94 MV/m—and the corresponding breakdown rates were 5.53×10^{-5}/pulse/m, 7.64×10^{-5}/pulse/m, and 1.62×10^{-4}/pulse/m, respectively. Figure 12 shows the measured breakdown rate in a semilogarithmic scale plot, where we can see that the gradient of this two-half structure is continuously increasing. The status of CLIC-G-Open at 3×10^7 pulses is a 90 ns pulse length, 55 MV/m gradient, and 2×10^{-4}/pulse/m [14]. The conditioning progress of the silver-brazed two-half structure is similar to that of CLIC-G-Open.

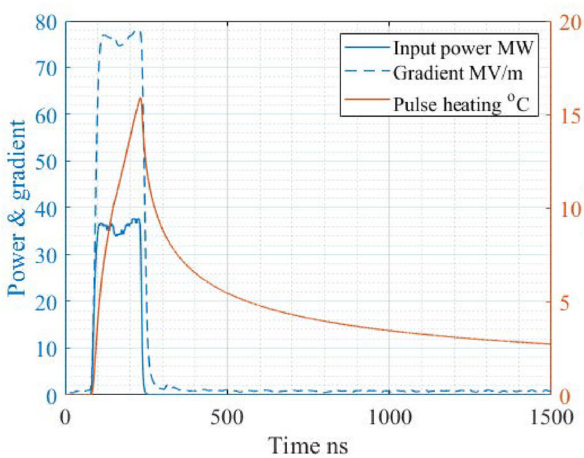

(a) Without pulse compressor

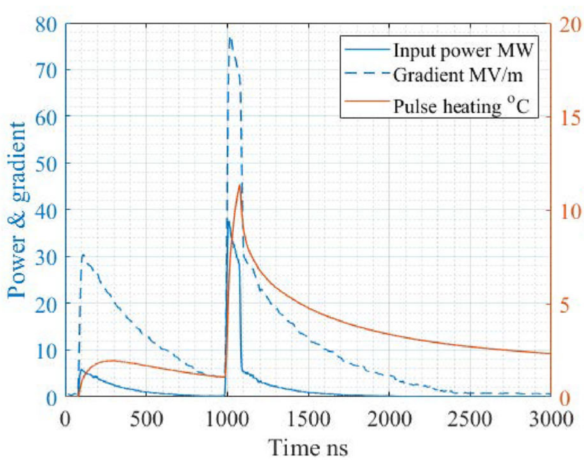

(b) With pulse compressor

Fig. 10 (Color online) Two-half structure input power, gradient, and surface pulse heating waveform. **a** Before pulse compressor installation and **b** after pulse compressor installation. Blue solid line: input power in MW. Blue dashed line: time-domain gradient in MV/m. Orange solid line: surface pulse heating in °C

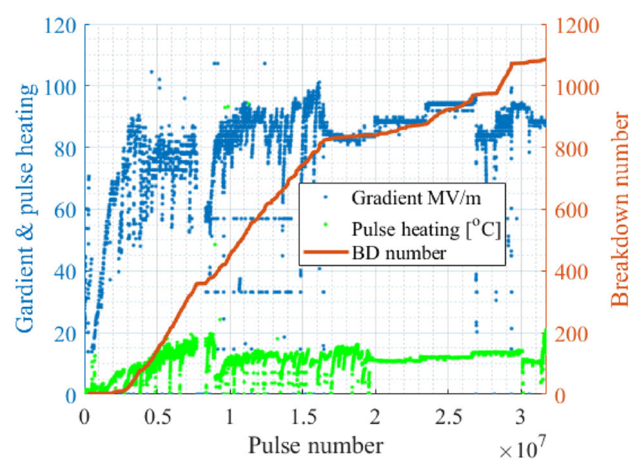

Fig. 11 (Color online) Condition history of two-half structure. There are a total of 3.17×10^7 pulses in the entire procedure. The maximum pulse width and gradient were 200 ns and 103 MV/m, respectively. A pulse compressor was installed at 0.8×10^7 pulses

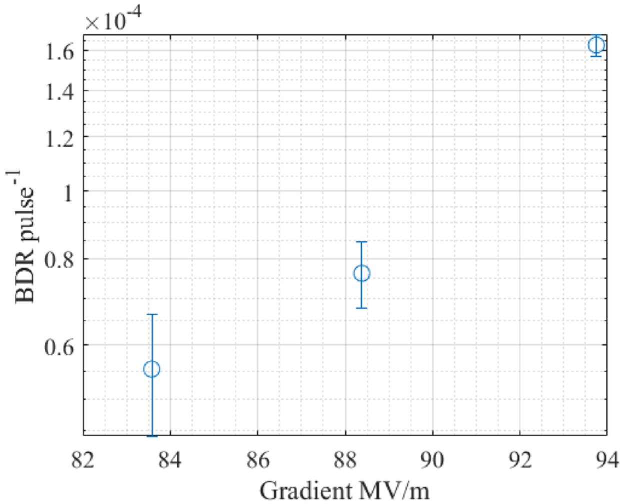

Fig. 12 Breakdown rate measurement of 3 different gradient

5 Conclusion

An X-band traveling wave two-half accelerator was designed and fabricated at Tsinghua University. This structure was brazed with a silver-based alloy and conditioned on a Tsinghua high-power test stand. The standing wave ratio of the on-axis electric field was 1.2, even without tuning. We measured the breakdown rate after the first cell gradient conditioning of 84 MV/m, 88 MV/m, and 94 MV/m, and the corresponding breakdown rates were found to be 5.53×10^{-5}/pulse/m, 7.64×10^{-5}/pulse/m, and 1.62×10^{-4}/pulse/m, respectively. The gradient of the two-half structure continuously increased as the conditioning time increased. Hence, compared with conventional room-temperature disk-loaded accelerator structures assembled by disks, the two-half structure has the potential of low price and advantages as a high-frequency linear accelerator, demonstrating promise for future applications.

Author Contributions All authors contributed to the study conception and design. Material preparation, data collection, and analysis were performed by Mao-Mao Peng, Jia-Ru Shi, Hao Zha, Xian-Cai Lin, Ze-Ning Liu, Yu-Liang Jiang, Jian Gao, Liu-Yuan Zhou, Fo-Cheng Liu, Xiang-Cong Meng, and Huai-Bi Chen. The first draft of the manuscript was written by Mao-Mao Peng, and all authors commented on previous versions of the manuscript. All authors read and approved the final manuscript.

References

1. M. Filtz, in: *Proceeding of European Particle Accelerator Conference, London*, Analytical calculation of waves in a muffin–tin structure. (1994), pp. 1271–1273
2. R. Sundelin, J. Kirchgessner, H. Padamsee et al., Application of superconducting rf accelerating sections to an electron synchrotron. a progress report. Technical report (1974)
3. R. Merte, Improved shape of an input/output wave guide with integrated taper for w-band muffin tin wband-003. Technical Note 140 (1998)
4. R. Merte, Improved design of w-band muffin tin wband-003. Technical Note 144 (1998)
5. P. Chou, G. Bowden, M. Copeland et al., in: *Proceedings of the 1997 Particle Accelerator Conference (Cat. No. 97CH36167)*, Design and fabrication of a traveling-wave muffin-tin accelerating structure at 90 ghz. Vol. 1, IEEE, (1997), pp. 464–466. https://doi.org/10.1109/PAC.1997.749688
6. S. Kuzikov, A. Fedotov, N.Y. Peskov et al., in: *AIP Conference Proceedings*, Millimeter and submillimeter-wave, high-gradient accelerating structures. Vol. 1812, AIP Publishing LLC, (2017), p. 060002. https://doi.org/10.1063/1.4975869
7. M. Dal Forno, V. Dolgashev, G. Bowden et al., Rf breakdown tests of mm-wave metallic accelerating structures. Phys. Rev. Accel. Beams **19**, 011301 (2016). https://doi.org/10.1103/PhysRevAccelBeams.19.011301
8. M. Dal Forno, V. Dolgashev, G. Bowden et al., High gradient tests of metallic mm-wave accelerating structures. Nucl. Instrum. Methods Phys. Res. Sect. A Accel. Spectrom. Detect. Assoc. Equip. **864**, 12–28 (2017). https://doi.org/10.1016/j.nima.2017.05.014
9. M. Dal Forno, V. Dolgashev, G. Bowden et al., Measurements of electron beam deflection and rf breakdown rate from a surface wave guided in metallic mm-wave accelerating structures. Phys. Rev. Accel. Beams **21**, 091301 (2018). https://doi.org/10.1103/PhysRevAccelBeams.21.091301
10. M.A. Othman, J. Picard, S. Schaub et al., Experimental demonstration of externally driven millimeter-wave particle accelerator structure. Appl. Phys. Lett. **117**, 073502 (2020). https://doi.org/10.1063/5.0011397
11. D. Palmer, M. Hill, S. Schwartzkopf et al., in: *Proceedings of the 1999 Particle Accelerator Conference (Cat. No. 99CH36366)*, Materials research related to w-band cavity construction. Vol. 1, IEEE, (1999), pp. 545–547
12. T. Abe, Y. Arakida, T. Higo et al., in: *International Workshop on Breakdown Science and High Gradient Technology (HG2015)* (Tsinghua University, China, Basic Study on High-Gradient Accelerating Structures at Kek/Nextef, 2015)
13. M. Aicheler, P. Burrows, M. Draper et al., A multi-TeV linear collider based on clic technology: CLIC conceptual design report. CERN, Geneva, Switzerland, Rep. CERN-2012-007 (2012). https://doi.org/10.5170/CERN-2012-007
14. T. Argyropoulos, N. Catalan-Lasheras, A. Grudiev et al., Design, fabrication, and high-gradient testing of an x-band, traveling-wave accelerating structure milled from copper halves. Phys. Rev. Accel. Beams **21**, 061001 (2018). https://doi.org/10.1103/PhysRevAccelBeams.21.061001
15. H. Zha, A. Grudiev, Design of the compact linear collider main linac accelerating structure made from two halves. Phys. Rev. Accel. Beams **20**, 042001 (2017). https://doi.org/10.1103/PhysRevAccelBeams.20.042001
16. H. Zha, J. Shi, H. Chen et al., Choke-mode damped structure design for the compact linear collider main linac. Phys. Rev. Spec. Top. Accel. Beams **15**, 122003 (2012). https://doi.org/10.1103/PhysRevSTAB.15.122003
17. X. Wu, J. Shi, H. Chen et al., High power test of x-band single cell hom-free choke-mode damped accelerating structure made by Tsinghua university. Technical report (2016) https://cds.cern.ch/record/2207494/files/thpor043.pdf
18. X. Wu, T. Abe, H. Chen et al., in: *8th International Particle Accelerator Conference (IPAC'17)*, Copenhagen, Denmark, 14–19 May, High-gradient breakdown studies of x-band choke-mode structures. JACOW, Geneva, Switzerland **2017**, 1322–1325 (2017)

19. V. Khan, A. D'Elia, R. Jones et al., Wakefield and surface electromagnetic field optimisation of manifold damped accelerating structures for clic. Nucl. Instrum. Methods Phys. Res. Sect. A: Accel. Spectrom. Detect. Assoc. Equip. **657**, 131–139 (2011). https://doi.org/10.1016/j.nima.2011.06.045
20. L. Laurent, S. Tantawi, V. Dolgashev et al., Experimental study of rf pulsed heating. Phys. Rev. Spec. Top. Accel. Beams **14**, 041001 (2011). https://doi.org/10.1103/PhysRevSTAB.14.041001
21. P. Zhang, Effects of surface roughness on electrical contact, rf heating and field enhancement. Ph.D. thesis (2012)
22. A. Grudiev, S. Calatroni, W. Wuensch, New local field quantity describing the high gradient limit of accelerating structures. Phys. Rev. Spec. Top. Accel. Beams **12**, 102001 (2009). https://doi.org/10.1103/PhysRevSTAB.12.102001
23. C.W. Steele, A nonresonant perturbation theory. IEEE Trans. Microw. Theory Tech. **14**, 70–74 (1966). https://doi.org/10.1109/TMTT.1966.1126168
24. M. Peng, D. Cao, W. Gai et al., in: *9th International Particle Accelerator Conference (IPAC'18)*, Vancouver, BC, Canada, April 29-May 4, Development of tsinghua x-band high power test facility. JACOW Publishing, Geneva, Switzerland **2018**, 3999–4001 (2018). https://doi.org/10.18429/JACoW-IPAC2018-THPAL150
25. Y. Jiang, J. Shi, P. Wang et al., in: *8th International Particle Accelerator Conference (IPAC'17)*, Copenhagen, Denmark, 14–19 May, The x-band pulse compressor for tsinghua thomson scattering x-ray source. JACOW, Geneva, Switzerland **2017**, 4214–4217 (2017)
26. X. Meng, H. Chen, C. Cheng et al., in: *7th International Particle Accelerator Conference (IPAC'16)*, Busan, Korea, May 8–13, Development of s-band high power load. JACOW, Geneva, Switzerland **2016**, 383–385 (2016)
27. X. Meng, J. Shi, H. Zha et al., Development of high-power s-band load. Nucl. Instrum. Methods Phys. Res. Sect. A Accel. Spectrom. Detect. Assoc. Equip. **927**, 209–213 (2019). https://doi.org/10.1016/j.nima.2019.02.002
28. J.Y. Liu, J.R. Shi, H. Zha et al., Analytic rf design of a linear accelerator with a sled-i type rf pulse compressor. Nucl. Sci. Tech. **31**, 107 (2020). https://doi.org/10.1007/s41365-020-00815-5
29. T. Higo, Y. Higashi, S. Matsumoto et al., in: *Conference on Proceedings C100523: THPEA013, 2010*, Advances in x-band tw accelerator structures operating in the 100 mv/m regime. No. SLAC-PUB-15150, SLAC National Accelerator Lab., Menlo Park, CA (United States), (2012)
30. A. Degiovanni, W. Wuensch, J.G. Navarro, Comparison of the conditioning of high gradient accelerating structures. Phys. Rev. Accel. Beams **19**, 032001 (2016). https://doi.org/10.1103/PhysRevAccelBeams.19.032001